Chen *et al. Journal of Nanobiotechnology* (2025) 23:342
https://doi.org/10.1186/s12951-025-03396-w

Journal of Nanobiotechnology

METHODOLOGY **Open Access**

Comprehensive wound healing using ETN@ Fe_7S_8 complex by positively regulating multiple programmed phases

Mengxia Chen[1,2†], Ting Liu[1,3†], Xiaonan Wang[4,5†], Lizeng Gao[4,6], Yunqing Cheng[2*], Jing Jiang[4*] and Jinhua Zhang[1*]

Abstract

Wound healing requires coordinated progression through multiple programmed phases including hemostasis, infection control, inflammatory resolution, proliferation, and tissue remodeling. Many nanomaterials have shown great potential to promote wound healing, however, most of them only address partial aspects of these processes, making a recovery hard with adequate effects. In this study, we prepared a complex of nano-iron sulfide integrated with erythrocyte-templated nanozyme (ETN) (ETN@Fe_7S_8) for comprehensive treatment of wounds. Firstly, ETN served as a mediator to confine iron sulfide to form Fe_7S_8 nanocomposite in a solvothermal reaction. Secondly, the ETN@Fe_7S_8 demonstrated bactericidal effects against methicillin-resistant *Staphylococcus aureus* (MRSA) by releasing ferrous iron and polysulfide to induce ferroptosis-like cell death. Thirdly, ferrous iron along with polysulfide exerted anti-inflammatory effects by inhibiting the activation of the NF-κB signaling pathway, while the polysulfide also contributed to angiogenesis by promoting the activation of vascular endothelial growth factor A (VEGFA), initiated phosphorylation-mediated activation of the PI3K/AKT signaling pathway, a master regulatory cascade governing endothelial cell survival, migration, and angiogenesis. When employed for wound, ETN@Fe_7S_8 showed the ability to prevent infection, reduce inflammation, promote angiogenesis, enhance cell proliferation, and remodel keratinocytes. Along with the hemostatic effect, ETN@Fe_7S_8 thus performed comprehensive effects for wound healing in the whole recovery stages. Therefore, our findings provide a multifunctional candidate of ETN and nano-iron sulfide complex which is capable of regulating and promoting wound healing.

[†] Mengxia Chen, Ting Liu and Xiaonan Wang contributed equally to this work.

*Correspondence:
Yunqing Cheng
chengyunqing1977@163.com
Jing Jiang
jiangjing@ibp.ac.cn
Jinhua Zhang
zhangjh@bjtu.edu.cn
[1] College of Life Science and Bioengineering, Beijing Jiaotong University, Beijing 100044, China
[2] School of Life Sciences, Jilin Normal University, Jilin 136000, China
[3] School of Life Science and Technology, Jinan University, Guangdong 510632, China
[4] Key Laboratory of Biomacromolecules, Institute of Biophysics, CAS Engineering Laboratory for Nanozyme, Chinese Academy of Sciences, Beijing 100101, China
[5] School of Life Sciences, University of Chinese Academy of Sciences, Beijing 101408, China
[6] Nanozyme Laboratory in Zhongyuan, School of Basic Medical Sciences, Zhengzhou University, Zhengzhou 450001, China

Graphical Abstract

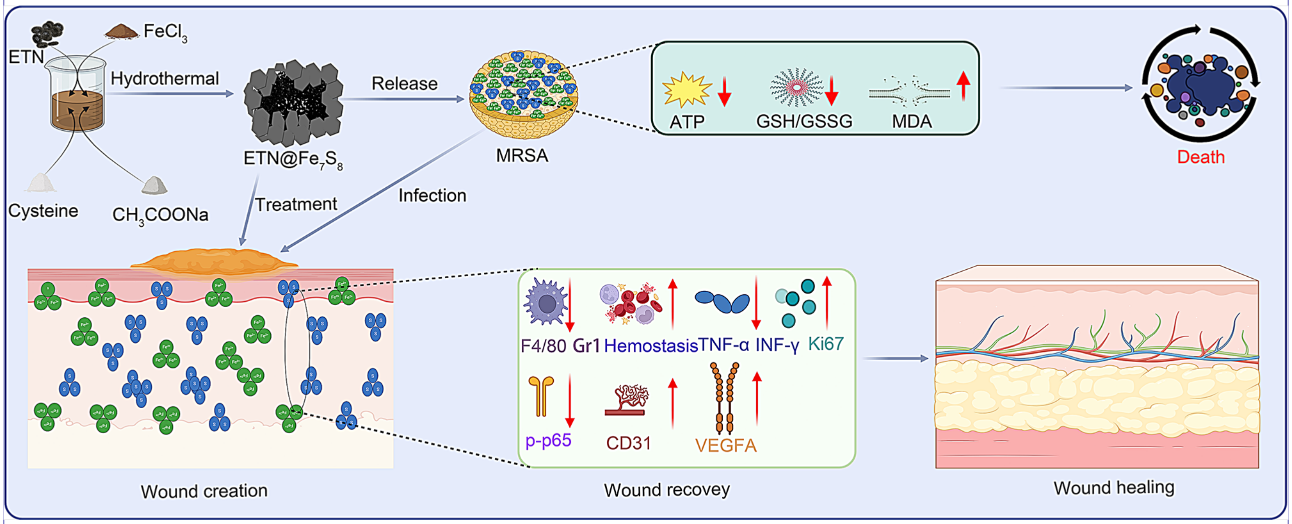

Keywords $ETN@Fe_7S_8$, Ferrous iron, Polysulfide, Anti-inflammatory effect, Angiogenesis

Introduction

Bacterial infections pose a substantial threat to global public health, leading to severe medical complications, increased mortality rates, and serious biosecurity risks [1, 2]. Antibiotics remain a cornerstone in combating bacterial infections and have saved countless lives [3, 4]. However, their inadequate and inappropriate use has resulted in the emergence of drug-resistant strains, such as multidrug-resistant bacteria, which acquire antimicrobial resistance (AMR) [5, 6]. Compared with 2022, the number of deaths attributed to AMR is projected to rise significantly, with an estimated increase of approximately 70% by 2050 [7]. Methicillin-resistant *Staphylococcus aureus* (MRSA) produces a distinctive penicillin-binding protein (PBP), PBP2a, which exhibits a low affinity for β-lactam antibiotics, rendering the bacteria resistant [8–10]. Bacteria are the etiologic agents of infections and infiltrate tissue layers [11, 12], leading to over 40% of chronic wound cases [13, 14]. Therefore, there is an urgent need to develop potent antibacterial agents to counteract the proliferation of antimicrobial-resistant bacteria.

Nanoparticles have garnered considerable attention because of their potential applications in treating various pathological conditions. They are synthesized through straight forward physical, chemical, and biological methods and are characterized by strong catalytic activity, high stability, and modifiable surfaces [15–17]. Gold nanoparticles (Au-NPs) bind to bacterial cell membranes, disrupting ion transport and ATP synthesis [18–20]. Silver nanoparticles (Ag-NPs) generate reactive oxygen species (ROS), which triggers bacterial cell apoptosis and prevents proliferation [21, 22]. Copper nanoparticles (Cu-NPs) kill bacteria directly and neutralize excessive ROS, thereby maintaining the microbial balance and amplifying their bactericidal effects [22–24]. However, nanoparticles may also exert significant cytotoxic effects on host cells, restricting restricts their broader application.

Murine erythrocytes subjected to salinization, lyophilization, and carbonization develop a loose and porous structure, resulting in the formation of erythrocyte-templated nanozyme (ETN) [25]. The Fe–N_4 coordination structure is dominant in ETNs and is considered the active site in oxygen-reduction catalysts, facilitating the formation of a stable composite structure [26, 27]. Although nanozymes based on copper or gold have shown promise in antibacterial applications, their reliance on expensive precursors, limited biocompatibility, or a single mechanism of action restricts their adaptability to complex wound environments. The peroxidase (POD)-like activity of ETN slightly inhibits bacterial viability, and when combined with the photothermal effect (PTT), it enhances bacterial cell damage, increasing mortality. However, the application of PTT is limited by the need for near-infrared (NIR) irradiation. In contrast, integrating iron sulfide and ETN introduces a multimodal antibacterial strategy that uniquely combines ferroptosis induction (via Fe^{2+}/polysulfide release) with enzymatic activity, and residual photothermal capacity, eliminating the strict dependence on NIR and outperforming single-functional iron-based or noble metal nanozymes.

Recent studies have demonstrated that iron sulfide nanomaterials effectively eliminate drug-resistant bacteria by releasing of ferrous iron and polysulfide, leading to ferroptosis in bacterial cells [28]. Moreover, these nanomaterials can circumvent drug resistance and exhibit broad-spectrum antibacterial efficacy [29, 30]. However, conventional iron-based nanozymes predominantly rely on fenton reaction-driven ROS generation or photothermal ablation, lacking sustained ion release kinetics and failing to regulate host tissue repair pathways simultaneously. Nanomaterials are increasingly being developed for applications in trauma treatment and angiogenesis. For example, the use of electrospun nanofibers can promote angiogenesis and neovascularization [31]. In particular, polyurethane (PU)/polycaprolactone (PCL) scaffolds are appropriate substrates for engineered vascular tissues under static and dynamic culturing of endothelial lineage [32], and heparinized PU/PCL composite nanofibers can enhance vascularization and endothelialization [33]. Although these platforms excel in vascularization, they exhibit negligible antibacterial activity against biofilm-embedded pathogens such as MRSA, a critical limitation in infected wound environments. Thus, existing strategies for treating chronic wounds often struggle to simultaneously tackle persistent bacterial infection, dysregulated inflammation, and impaired tissue regeneration, limiting their clinical utility. Our study addresses this challenge by engineering a nanocomposite containing iron sulfide. We hypothesized that integrating iron sulfide nanomaterials into a multifunctional nanocomposite could enhance antibacterial efficacy and actively promote wound healing. In this study, we synthesized an iron sulfide ETN nanocomposite (ETN@Fe_7S_8) using a hydrothermal approach. Our study aims to address two critical questions: (1) Can ETN@Fe_7S_8 overcome the limitations of conventional antibacterial agents with their pro-healing functions? (2) How do its two mechanisms regulate microbial eradication and host tissue responses? As shown in Scheme 1, ETN@Fe_7S_8 exerts a profound biological effect by releasing

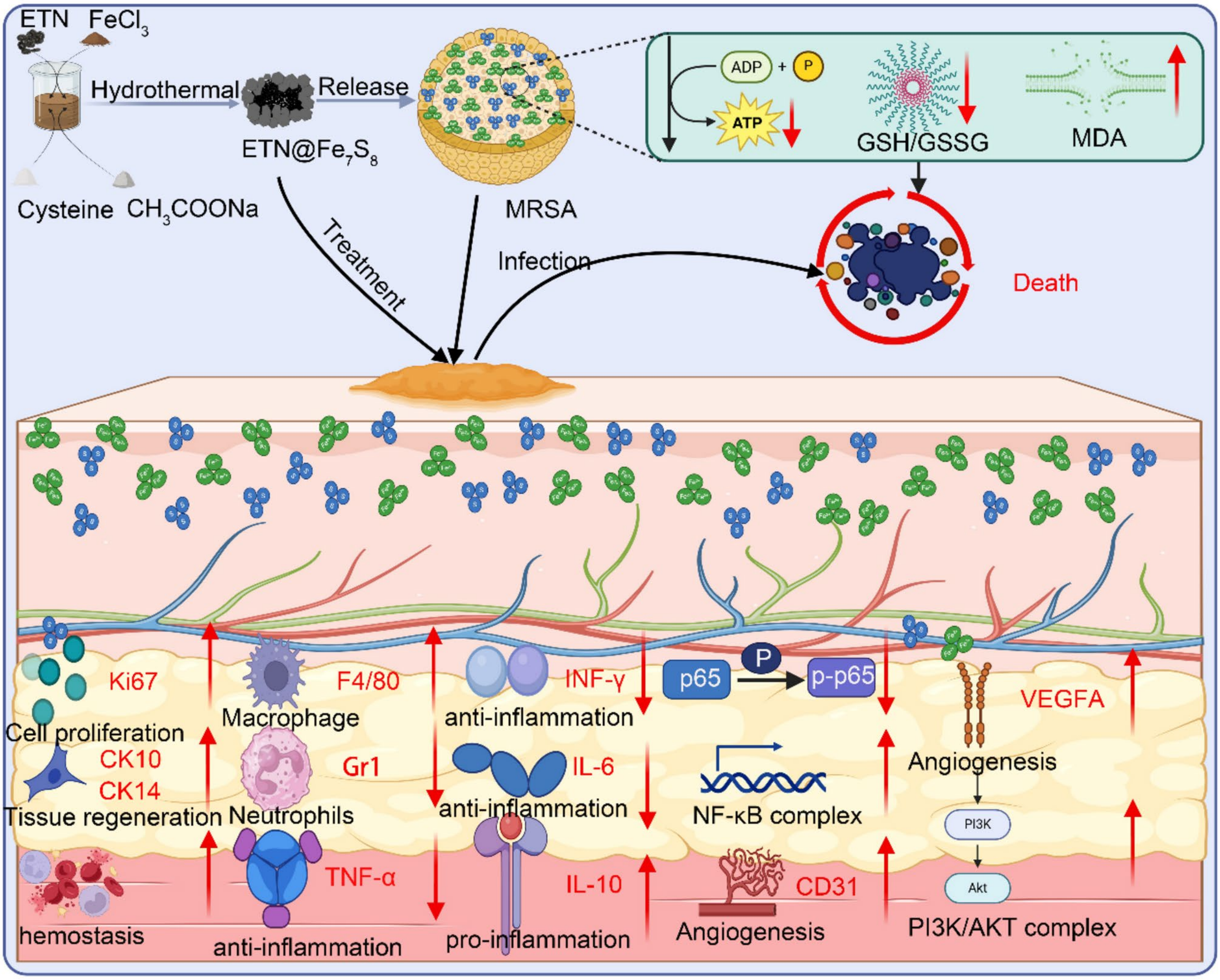

Scheme 1 Synthesis of ETN@Fe_7S_8 and its application and mechanism in an MRSA-infected wound

ferrous iron and polysulfide, which influence metabolism, promote lipid peroxidation, exhaust glutathione (GSH), mitigate inflammation by engaging the NF-κB signaling pathway, promote angiogenesis by stimulating the migration of human umbilical vein endothelial cells (HUVECs), and activate the PI3K/AKT-mediated pro-angiogenic signaling pathway. Furthermore, ETN@Fe_7S_8 exhibits superior biocompatibility, indicating its potential as a novel antibacterial candidate for managing wounds compromised by bacterial infections.

Experimental section

Reagents and materials

Mouse anticoagulant whole blood from Bersee (Beijing, China), Ferric chloride ($FeCl_3$), cysteine, sodium acetate trihydrate ($NaAc·3H_2O$), ethylene glycol, NaCl, and ferrous chloride ($FeCl_2$) were obtained from Sigma-Aldrich (USA). SulfoBiotics-SSP4 from DOJINDO (Japan). Yeast extract, glucose, starch, and drug-sensitive pieces were obtained from Oxoid (UK). Agar was purchased from Sangon Biotech (Shanghai, China). The cell counting kit-8 was acquired from Aladdin Chemistry (Shanghai, China). The iron content kit was sourced from Solarbio (Beijing, China). The malondialdehyde kit was purchased from Nanjing Jiancheng Bioengineering Institute (Nanjing, China). The GSH and glutathione disulfide (GSSG) assay kit, ATP assay kit, and propidium iodide (PI) were obtained from Beyotime Biotechnology (Shanghai, China). SYTO 9 was acquired from Thermo Fisher Scientific (Waltham, MA). MRSA was obtained from American Type Culture Collection (ATCC) (USA). More details of primary materials and antibodies used in the study are shown in Table S1.

Materials synthesis and characterization

Synthesis of ETN@Fe_7S_8

ETN@Fe_7S_8 was synthesized via a hydrothermal method: 30 mg ETNs in 30 mL ethylene glycol, stirred 2 h, sonicated 10 min, then 324.4 mg $FeCl_3$ added and stirred 1 h. After adding 3.6 g $NaCH_3COOH·3H_2O$ and stirring 30 min, 0.5 g cysteine was added and stirred overnight. The mixture was heated at 200 °C for 12 h, cooled, washed with ethanol and water, and dried using vacuum freeze-drying. The product was collected in 1.5 mL EP tubes.

Characterization of ETN@Fe_7S_8

A 10 μL solution was added to a smooth silicon chip and dried using a critical point dryer for scanning electron microscope (SEM) (Hitachi SU8010, Japan). High-Angle Annular Dark Field (HAADF) was employed to observe lattice fringes and perform electron selective diffraction, while energy-dispersive X-ray spectroscope (EDS) was utilized for elemental analysis. Characterization was conducted using an X-ray diffractometer (XRD) with the D8 ADVANCE model. The Raman spectra was obtained using a Renishaw 1000 micro-Raman system. The nitrogen (N_2) absorption-desorption results were collected at 77 K using a micromeritics instrument.

Identification of iron and polysulfide released from ETN@Fe_7S_8

ETN@Fe_7S_8 was mixed with water to a 1 mg/mL concentration and sonicated for 10 min. After settling for 30 min, it was centrifuged at 10,000 g for 10 min. The iron content in the supernatant was measured using an iron assay kit. In addition, the supernatant was diluted to 50, 100, and 200 μg/mL concentrations, and 1 μL of SSP4 probe was added to each for fluorescence measurement using a spectrometer, which determined the polysulfide levels.

In vitro methodologies

In vitro antibacterial assays

MRSA cultures were propagated in Luria Bertani (LB) medium under standard conditions (37 °C, 180 rpm) until reaching mid-log phase (OD600 = 0.5), diluted the as-prepared bacteria solution to 0.01, then added 100 μL bacteria solution into 900 μL different materials (H_2O, ETN, $Fe_{1-x}S$, vancomycin, and ETN@Fe_7S_8) or different concentration of ETN@Fe_7S_8 (0, 125, 250, 500 μg/mL) for 30 min. Treated samples were then spread-plated on LB agar and incubated for 14–16 h at 37 °C. Colony-forming units (CFUs) were quantified using a Tanon ChemiScope imaging system. (Tanon, China).

For metabolic profiling, MRSA was cultured to late-log phase (OD600 = 0.6–0.8) and treated with H_2O, ETN, $Fe_{1-x}S$, ETN@Fe_7S_8, $FeCl_2$, or Na_2S_4 under identical conditions. Following 30 min incubation, bacterial pellets were harvested by centrifugation (10,000 g, 10 min), washed with PBS, and lysed via sonication (15 min, 4 °C) in ATP/GSH/MDA-specific extraction buffers. cellular ATP levels, GSH/GSSG, and MDA were quantified using commercial kits (Beyotime Biotechnology, Solarbio) according to manufacturer protocols.

Live/dead staining test

MRSA was treated with H_2O, ETN, $Fe_{1-x}S$, and ETN@Fe_7S_8 for 30 min, respectively. The bacterial cells were centrifugated to collect sediment and stained with SYTO 9 (green) for 20 min in the dark for live cells, washed with PBS and then stained with PI (red) for 20 min in the dark for dead cells and were analyzed using a laser confocal microscope (OLYMPUS FV1000) to distinguish between live (green) and dead (red) cells based on their fluorescence properties.

MRSA morphology detection with SEM

MRSA with different treatments was resuspended in glutaraldehyde (2.5%, Sigma-Aldrich) for 24 h at 4 °C in the dark. The bacteria were then washed and dehydrated with a graded ethanol solution (30%, 50%, 70%, 90%, and 100%). A critical point dryer was used and the samples were coated with platinum vis sputtering. Finally, SEM images were obtained using a Hitachi S-4800 FE-SEM at a working voltage of 15.0 kV and a working current of 10 μA, under a magnification of 40 K.

MRSA morphology detection with TEM

MRSA with different treatments was resuspended in a 1% osmium tetroxide fixative solution for 24 h at 4 °C in the dark, then washed with PBS. The bacteria were dehydrated sequentially in 50%, 70%, and 90% ethanol, and a 1:1 mixture of 90% ethanol and 90% acetone, followed by 90% acetone and 100% acetone, with each solution applied three times. The samples were then soaked in acetone. Curing was performed in an over at different temperatures (37 °C overnight, and 45 °C and 60 °C for 12 h). The samples were sliced using an ultramicrotome and stained with uranium acetate and lead citrate. Finally, TEM images were obtained using a JEOL microscope.

Cell culture

HUVECs, Human keratinocyte cells (HaCaT), and mouse mononuclear macrophage cells (Raw264.7) were cultivated in Dulbecco's Modified Eagle Medium (DMEM) containing a high concentration of glucose, which was supplemented with 10% fetal bovine serum (FBS) and 1% penicillin-streptomycin solution. The cells were maintained in a controlled environment with 5% carbon dioxide (CO_2) at 37 °C.

Cell proliferation assay

In this study, HUVECs and Raw264.7 cells were seeded into 96-well plates at a density of 1×10^4 cells and 1.5×10^4 cells per well, respectively. The cells were cultured for 24–48 h. Subsequently, 100 μL of samples at varying concentrations ETN@Fe_7S_8 (0, 100, 200, 300, 400, and 500 μg/mL), $FeCl_2$ (0, 100, 200, 300, 400,500, and 1000 μM), Na_2S_4 (0, 10, 20, 30, 40, 50, and 100 μM) were added to each well. The proliferative activity was detected by Methylthiazolyidipihenyl-tetrazolium bromide (MTT) according to the manufacturer's protocols. The OD490 value of cells was analyzed at 0 and 24 h.

Trans-well chamber assay

HUVECs, adjusted to a density of 8×10^3 cells were plated in the upper chamber of the trans-well apparatus, while DMEM, ETN, $Fe_{1-x}S$, and ETN@Fe_7S_8 were added to the lower chamber. After 48 h, the cells in the upper chamber were removed, and the remaining cells were fixed with paraformaldehyde and stained with crystal violet. Excess dye was washed then washed away with PBS, and, optical images were subsequently captured.

Scratch assay

HaCaT cells were seeded at a density of 2×10^5 adherence in 12-well plates, a linear wound was created using the tip of a 200 μL pipette, the cell debris was then washed away with PBS. Subsequently, different materials ETN, $Fe_{1-x}S$, and ETN@Fe_7S_8 (500 μg/mL) were added and the cells were incubated for 0, 12, 24 and 48 h, optical images were captured at each time point.

After HUVECs were seeded at a density of 2×10^5 adherence in 12-well plates, a linear wound was created using the tip of a 200 μL pipette, the cell debris was then washed away with PBS. Subsequently, ETN@Fe_7S_8 (100 μg/mL), $FeCl_2$ (100 μM), and Na_2S_4 (20 μM) were added and the cells were incubated for 0 and 24 h, optical images were captured at each time point.

Tube formation assay of HUVECs

Incubated HUVECs with DMEM, ETN, $Fe_{1-x}S$, ETN@Fe_7S_8, $FeCl_2$, and Na_2S_4. After 24 h, 2×10^4 cells were added to each well containing Matrigel (Solarbio, China). Images were captured using an optical microscope, and ImageJ software was utilized to quantify the length and formation of the tubules.

Biocompatibility and toxicity assessment

Cytotoxicity assays

To assess the biocompatibility of ETN@Fe_7S_8, Raw264.7, and HaCaT cells were seeded at a density of 5×10^4 cells per well in 96-well assay plates overnight and then treated with prepared samples for 24 h. To evaluate toxicity, 10 μL of the cell counting cit-8 (CCK-8) solution was added to each well and incubated in a 5% CO_2 environment for 2 h. Subsequently, the absorbance values were measured using a microplate reader at a wavelength of 450 nm.

Blood compatibility

Briefly, 1 mL of fresh anticoagulated whole blood from mice was diluted with 5 mL of PBS, and centrifuged at 10,000 g for 5 min. The erythrocytes were washed with PBS and then resuspended in 10 mL of PBS. A total of 100 μL of the erythrocyte suspension was added to 400 μL of various samples (H_2O, PBS, and concentrations of 125, 250, 500, and 1000 μg/mL ETN@Fe_7S_8) and incubated at 37 °C for 4 h. All mixed solutions were then centrifuged at 10,000 g for 5 min. Subsequently, the supernatants were measured at 577 nm using a microplate reader ($n = 3$). H_2O and PBS served as the negative and positive controls, respectively.

ELISA assay

On day 7 of wound healing, the wound tissues were harvested and ground. The supernatant was collected and used for subsequent ELISA analysis. The TNF-α ELISA kit and IFN-γ ELISA kit were purchased from BIOSs (Shanghai, China). All tests were conducted according to the manufacturer's instructions.

Quantitative real-time polymerase chain reaction (qPCR)

Total RNA was isolated from wound tissue or Raw264.7 cells using the RNeasy Mini Kit (QIAGEN, Dusseldorf, Germany) following the manufacturer's instructions. 500 ng of RNA was reverse transcribed to cDNA using a FastKing RT kit (with gDNase) (TIANGEN, China) in a thermal cycler (Takara, Japan). Real-time quantitative PCR (RT-qPCR) was conducted using SYBR Green qPCR Master Mix (TIANGEN, China). β-actin was utilized as the endogenous reference gene for normalization. The formula for the relative expression value was as follows: $2^{(-\triangle\triangle Ct)}$. The gene-specific primers used are presented in Table S2.

Western blot analysis

Raw264.7 cells were seeded in 6-well plates at a density of 5×10^5 cells per well and stimulated with LPS (100 ng/mL), ETN@Fe_7S_8 (100 μg/mL), $FeCl_2$ (100 μM), and Na_2S_4 (20 μM). Following a 24-hour incubation, cell extracts were using the following primary antibodies: anti-p65, anti-p-p65 (ProteinTech, Chicago, IL, USA), and β-actin (Santa Cruz Biotechnology, CA, USA). HRP-conjugated goat anti-mouse or goat anti-rabbit IgG was used as secondary antibodies.

HUVEC cells were seeded in 6-well plates at a density of 5×10^5 cells per well and stimulated with ETN@Fe_7S_8 (100 μg/mL), $FeCl_2$ (100 μM), and Na_2S_4 (20 μM). Following a 24-hour incubation, cell extracts were using the following primary antibodies: anti-VEGF, anti-AKT, anti-P-AKT, anti-PI3K, and P-PI3K (Affinity Biosciences. OH. USA). HRP-conjugated goat anti-mouse or goat anti-rabbit IgG was used as secondary antibodies.

In vivo methodologies

Mouse wound model

All animal studies were conducted in accordance with the protocols approved by the Institutional Animal Care and Use Committee of the Institute of Biophysics, Chinese Academy of Sciences. Female Balb/c mice (aged 8 to 10 weeks) were obtained from Huafukang Biotechnology Co. Ltd.

To evaluate the antibacterial properties of ETN@Fe_7S_8 in vivo, a wound model was developed. The 36 female Balb/c mice, each with a wound approximately 10 mm², and were divided into six groups: PBS, Uninfected, ETN, $Fe_{1-x}S$, Vancomycin, and ETN@Fe_7S_8. A 30 μL suspension of MRSA (5×10^7 CFU) was applied to the center of each wound and allowed to incubate for 24 h. Subsequently, 20 μL of the different materials dispersed in PBS (1 mg/kg) were topically spread over the entire wounds for once. Photographs of the wounds and the weights of the mice were recorded daily.

In vivo hemostatic ability assay

In the rabbit auricular vein hemorrhage model, rabbits were intravenous injected of 10% ethyl carbamate solution to anesthetize. Following the induction of anesthesia, the auricular veins of the rabbits were transected using a scalpel, and absorbent cotton pledgets with 500 μg/mL ETN@Fe_7S_8 were applied to the incision sites. The time required for hemostasis and the quantity of blood loss were accurately recorded.

In the mouse liver hemorrhage model, mice were intraperitoneal injection 10% ethyl carbamate solution to anesthetize, an incision was made at the thoracic septum using forceps and scissors to expose the liver. A part of hepatic tissue was excised with scissors, and absorbent cotton pledgets with 500 μg/mL ETN@Fe_7S_8 were positioned over the hepatic wound. The time required for hemostasis and the quantity of blood loss were accurately recorded.

Histology and immunostaining

On days 3 and 7 of wound healing, the wound tissues were harvested. Following deparaffinization and rehydration, the tissue slices were stained with hematoxylin and eosin (H&E) for histological observation. For immunofluorescence staining, sections from different groups were incubated with anti-Gr1, anti-Ki67, and anti-F4/80 antibodies (BD Pharmingen, San Diego, CA, USA), anti-CD31, anti-CK10, and ant-CK14 antibodies (Affinity Biosciences, USA), followed by Alexa Fluor 488- and 594-conjugated secondary antibodies (Jackson ImmunoResearch Labs, Carlsbad, CA). Sections were evaluated under a microscope (DP71, OLYMPUS) for brightfield and fluorescence microscopy.

Statistical assay

All data presented in this article are expressed as mean results ± standard deviation (SD) and were analyzed by the GraphPad Prism V8.0 software. The difference between the two groups was compared by two-tailed unpaired Student's t-test. Multiple comparisons were made using two-way ANOVA analysis. The data are representative of at least three independent experiments. $P < 0.05$ was considered statistically significant.

Results and discussion

Synthesis and characterization of ETN@Fe_7S_8

In this study, we prepared a novel nanocomposite material, ETN@Fe_7S_8, that integrates iron sulfide with ETNs to target MRSA. ETN@Fe_7S_8 was synthesized via hydrothermal method, and the process is presented in Fig. 1A. Subsequent morphological characterization using SEM and HAADF imaging revealed the intricate composite

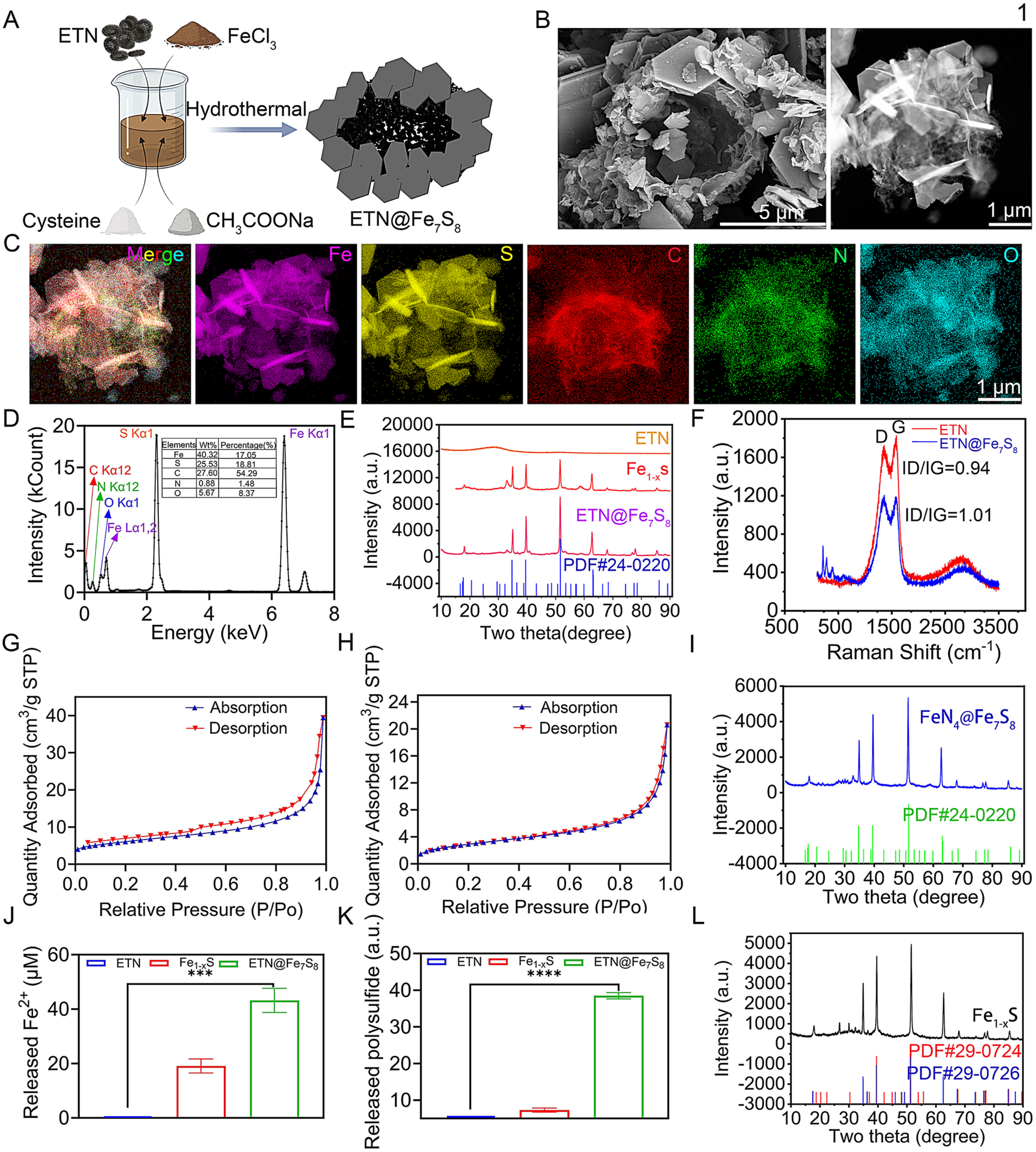

Elements	Wt%	Percentage(%)
Fe	40.32	17.05
S	25.53	18.81
C	27.60	54.29
N	0.88	1.48
O	5.67	8.37

Fig. 1 Synthesis and characterization of ETN@Fe_7S_8. (**A**) Schematic illustration of the synthesis of ETN@Fe_7S_8. (**B**) SEM and HAADF images of ETN@Fe_7S_8. (**C**) EDS mapping images of ETN@Fe_7S_8. (**D**) EDS analysis of elements in ETN@Fe_7S_8. (**E**) XRD pattern of ETN, $Fe_{1-x}S$, and ETN@Fe_7S_8. (**F**) Raman spectra of ETN (red curve) and ETN@Fe_7S_8 (blue curve). (**G**) N_2 absorption and desorption curves for ETN. (**H**) N_2 absorption and desorption curves for ETN@Fe_7S_8. (**I**) XRD pattern of FeN_4@Fe_7S_8. (**J**) Ferrous iron released from different materials. (**K**) Polysulfides released from different materials. (**L**) XRD pattern after the release of ferrous iron and polysulfide. $***P < 0.001$, $****P < 0.0001$

architecture of ETN@Fe_7S_8 (Fig. 1B), with the ETN at the center (Fig S1), surrounded by $Fe_{1-x}S$ (Fig S2). Elemental mapping, using energy-dispersive X-ray (EDS) [34], indicated that the nanocomposite predominantly comprised iron (Fe), sulfur (S), carbon (C), nitrogen (N), and oxygen (O) (Figs. 1C-D). The corresponding elements analysis confirmed the presence of $Fe_{1-x}S$ loaded onto the ETN (Figs S3 and S4). The crystallographic structure and phase purity of the synthesized nanocomposite were rigorously characterized by XRD, the peaks at 2θ of 18, 34.9, 39.6, 51.5, 62.7, 68, 76.9, 77.9 and 85.5° represented diffractions from Fe_7S_8 (ICCD PDF#24–0220) (Fig. 1E). Raman spectra revealed that the I_D/I_G ratios for ETN and ETN@Fe_7S_8 were 0.94 and 1.01, respectively, indicating that ETN@Fe_7S_8 has more defects than ETN owing to the incorporation of the $Fe_{1-x}S$ dopant (Fig. 1F and Table S3). The N_2 adsorption/desorption experiment confirmed the surface area and pore size of ETN and ETN@Fe_7S_8. ETN@Fe_7S_8 exhibited smaller adsorption/desorption characteristics than ETN (Figs. 1G-H), indicating that the structure of ETN was altered by the second heat treatment. The Brunauer–Emmett–Teller (BET)-specific surface areas of ETN, $Fe_{1-x}S$, and ETN@Fe_7S_8 were measured at 20.72, 12.65, and 10.17 m^2/g, respectively. The Barrett–Joyner–Halenda (BJH) method revealed that the pore volume and size were 0.05 cm^3/g and 10.28 nm for ETN, 0.05 cm^3/g and 16.17 nm for $Fe_{1-x}S$, and 0.03 cm^3/g and 11.63 nm for ETN@Fe_7S_8, respectively, indicating that the gap in ETN increased due to $Fe_{1-x}S$ doping (Table S4).

ETN was replaced with a carbon ball composed of FeN_4 to determine the role of ETN in the preparation of the ETN@Fe_7S_8 nanocomposite [35–37]. At the same concentration of FeN_4 and ETN, the formation of a Fe-N_4@Fe_7S_8 composite was observed. Therefore, we hypothesized that the ETN framework provides a Fe-N_4 coordination site for binding sulfide species, promoting the assembly of the ETN@Fe_7S_8 structure. This interaction is crucial for stabilizing the composite and enhancing its functional properties (Fig. 1I). In addition, we assessed the ability of ETN@Fe_7S_8 to release ferrous iron and polysulfide, characteristics that contribute to its antibacterial effects [38, 39]. The results indicated that ETN@Fe_7S_8 released 45 μM of ferrous iron, which was higher than that released by $Fe_{1-x}S$ (Fig. 1J). The release of polysulfide was consistent with that of ferrous iron (Fig. 1K). After the release of ferrous iron and polysulfide, the residual components corresponded to different $Fe_{1-x}S$ crystals (Fig. 1L). Overall, the results highlight the unique interplay between the ETN template and iron sulfide, which culminated in the formation of the ETN@Fe_7S_8 nanocomposite with enhanced therapeutic potential.

ETN@Fe_7S_8 triggers MRSA elimination through ferrous iron-mediated cellular damage

Based on the presence of ferrous iron and polysulfide, the antibacterial effects were further evaluated. The antibacterial effects of ETN@Fe_7S_8 were initially evaluated using a colony-counting methodology. The groups treated with ETN and $Fe_{1-x}S$ exhibited moderate antibacterial activities, whereas the group treated with ETN@Fe_7S_8 showed a pronounced reduction in colony-forming units (CFU), with bacterial viability of 3.03 ± 0.05, which equates to an approximate killing rate of 99% (Fig. 2A-B), indicating that the antibacterial effect is better than that of the positive control vancomycin. Furthermore, the antibacterial effect of ETN@Fe_7S_8 was assessed at different concentrations, and the results indicated that at a concentration of 500 μg/mL, approximately 99.9% of MRSA was killed (Fig S5); thus, this concentration was used for subsequent experiments. Bacterial survival was further evaluated using a live/dead staining assay (SYTO 9 and PI). Consistent with previous studies, ETN@Fe_7S_8 caused the most severe damage, as evidenced by the highest number of nonviable bacteria (Fig. 2C). In addition, the cytosolic membrane of MRSA cells in the ETN@Fe_7S_8 group was markedly damaged, whereas the $Fe_{1-x}S$ group exhibited only slight damage. In contrast, minimal morphological alterations were detected in the control and ETN groups (Fig. 2D).

Iron sulfide nanomaterials effectively eliminate drug-resistant bacteria by releasing ferrous iron and polysulfide. Ferrous iron enters bacterial cells through divalent metal transporters (DMTs) [40], leading to ferroptosis in bacterial cells [28, 41]. Polysulfide forms stable complexes with ferrous ions, preventing their oxidation to ferric ions [42]. We used $FeCl_2$ and Na_2S_4 as sources for ferrous iron and polysulfide, respectively, to evaluate variations in MRSA. The ATP concentrations in the ETN@Fe_7S_8, $FeCl_2$, and Na_2S_4 groups were markedly decreased, whereas those in the $Fe_{1-x}S$ group were partially decreased (Fig. 2E). Furthermore, ETN@Fe_7S_8 and $FeCl_2$ catalyzed lipid peroxidation of the membrane (Fig. 2F). Moreover, the balance between GSSG and reduced GSH was disrupted (Fig. 2G). Overall, ETN@Fe_7S_8 exhibits exceptional antibacterial characteristics against MRSA. Polysulfide synergizes with ferrous iron to induce bacterial cell death, leading to membrane disintegration, metabolic inhibition, GSH depletion, and enhanced lipid peroxidation (Fig. 2H). These results indicate the potential of ETN@Fe_7S_8 as a powerful antibacterial agent capable of neutralizing MRSA primarily through the bactericidal effects of ferrous iron.

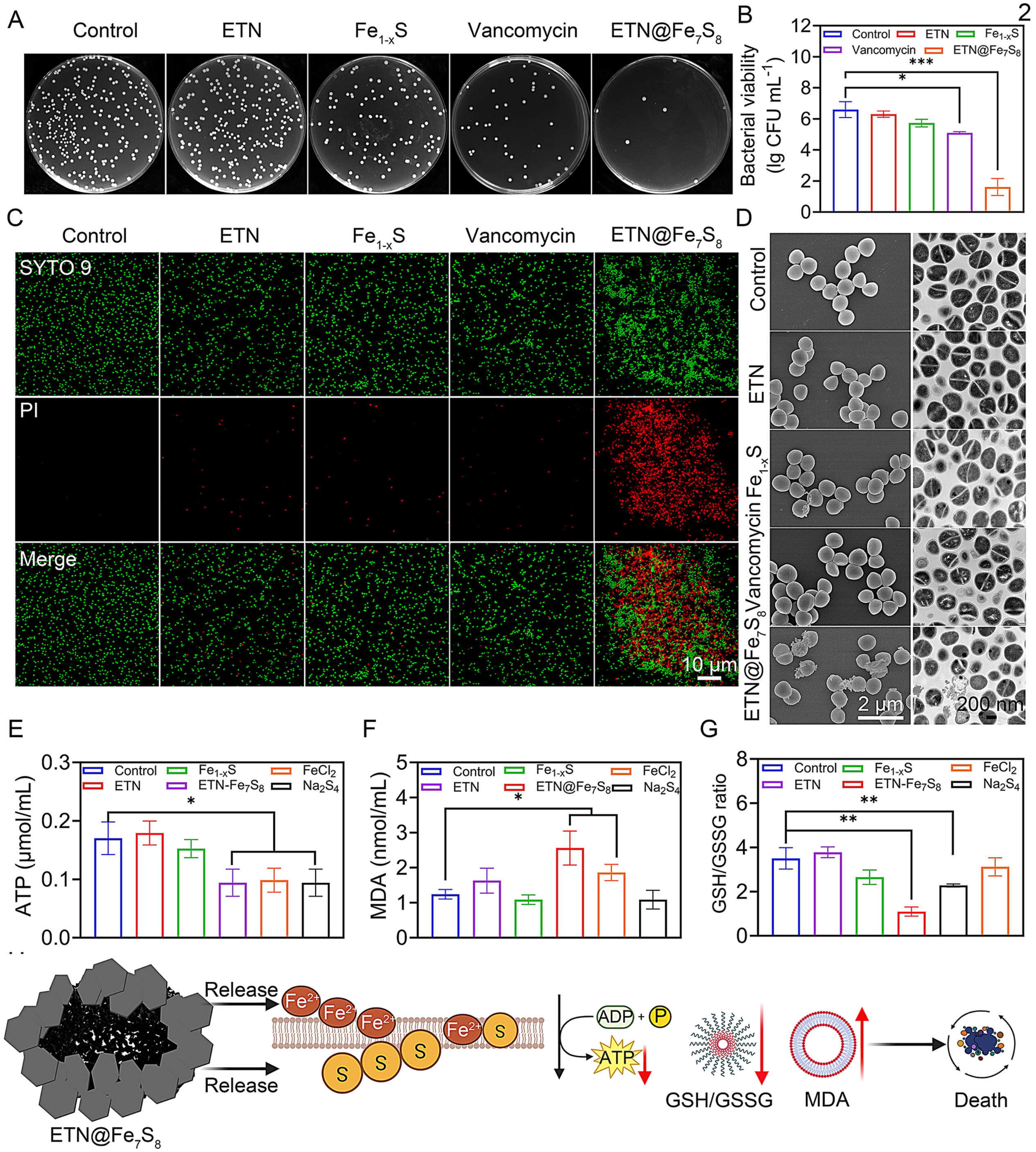

Fig. 2 In vitro antibacterial performance of $ETN@Fe_7S_8$. (**A**) Photographs of bacterial colonies of MRSA in different treatments. (**B**) Bacterial viability of MRSA following different treatments. (**C**) Live/Dead fluorescence images of MRSA after different treatments. (**D**) SEM and TEM images of MRSA in different treatment groups. (**E**) ATP production of MRSA in different treatments. (**F**) Lipid peroxidation of MRSA in different treatments. (**G**) The GSH/GSSG ratio in MRSA in different treatments. (**H**) A schematic summary of the antibacterial mechanisms. $*P < 0.05$, $**P < 0.01$, $****P < 0.0001$

Accelerating wound healing in MRSA infections: the efficacy of $ETN@Fe_7S_8$ nanocomposite

To determine the effectiveness of $ETN@Fe_7S_8$ in a living model with MRSA infection, an in vivo study was conducted using female Balb/c mice. A 1-cm diameter wound was surgically created on the backs of the mice and inoculated with MRSA at a density of 5×10^7 CFU per wound. The infection model was confirmed to be successfully established once a clear yellow discoloration was observed at the wound site (Fig. 3A). The mice

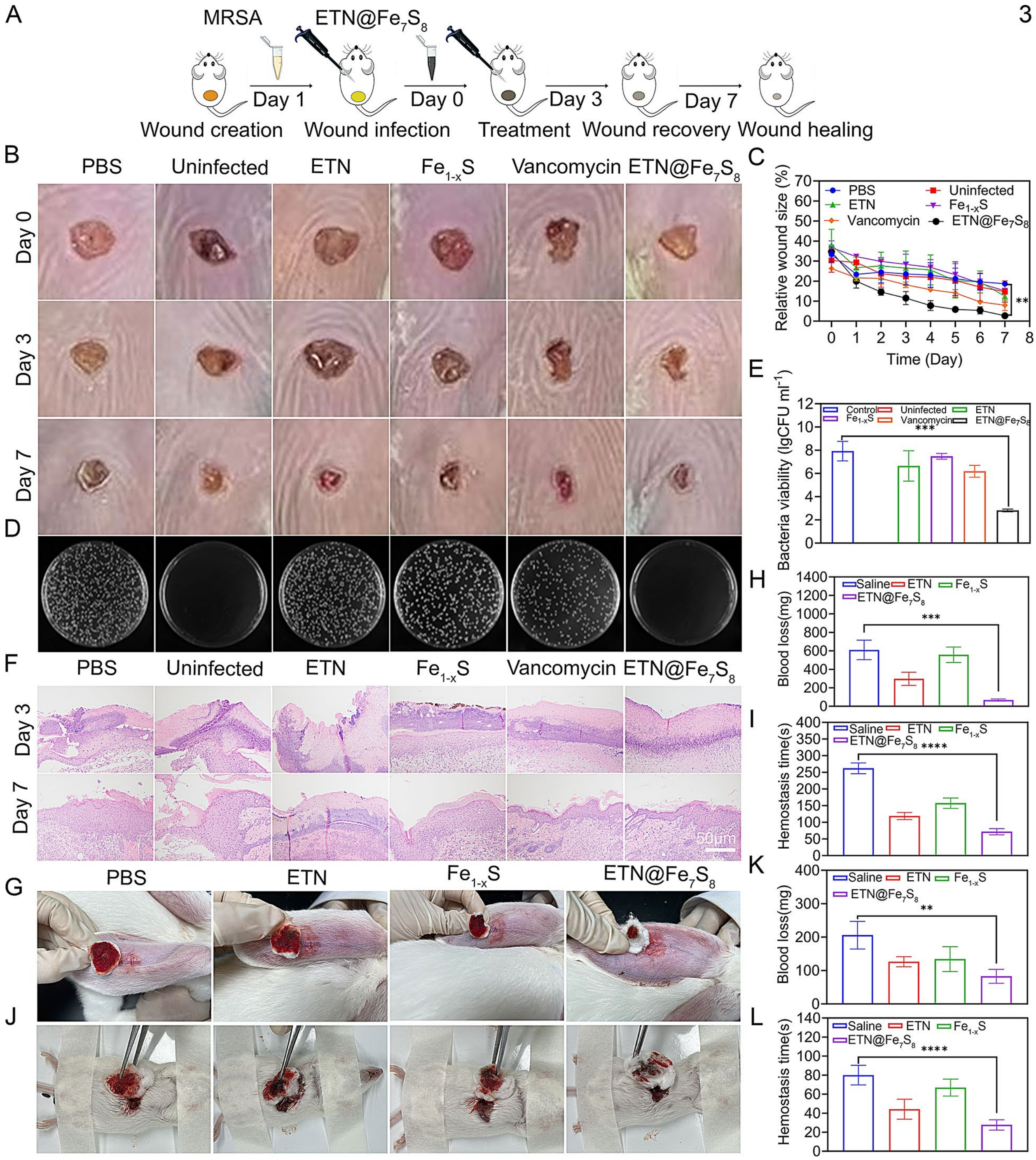

Fig. 3 $ETN@Fe_7S_8$ promotes wound healing and clotting in vivo. (**A**) Antibacterial treatment paradigm in murine model. (**B**) Wound images of mice after various treatments at different times. (**C**) Relative wound size. (**D**) Photographs of bacterial colonies after 7 days of treatment. (**E**) Bacterial viability of MRSA after different treatments. (**F**) H&E staining of the bacteria-infected tissues after different treatments. (**G**) Representative images of rabbit auricular vein hemorrhage, and (**H–I**) procoagulant effects of $ETN@Fe_7S_8$. (**J**) Representative images of mouse liver hemorrhage, and (**K–L**) procoagulant effects of $ETN@Fe_7S_8$. $^{**}P < 0.01$, $^{***}P < 0.001$, $^{****}P < 0.0001$

were randomly divided into the following six groups: (1) PBS (negative control to assess baseline healing without treatment); (2) Uninfected (to exclude nonspecific wound responses); (3) ETN (to evaluate the standalone nanozyme's activity); (4) $Fe_{1-x}S$ (to isolate the effects of the iron sulfide precursor); (5) Vancomycin (positive control, a first-line antibiotic for MRSA); and (6) $ETN@Fe_7S_8$. Figures 3B-C showed representative images of the infected wounds and provide a quantitative analysis of the wound sites. The wounds treated with ETN@Fe_7S_8 showed marked improvement in healing and a substantial decrease in size compared with those in other treatment groups on day 7 and were comparable to those in the vancomycin-treated group. The lack of significant weight changes in the mice indicated that there were no severe adverse effects associated with the infection (Fig S6).

We assessed MRSA by counting the bacterial colonies on day 7 post-treatment. As shown in Figs. 3D-E, the CFU values in the ETN@Fe_7S_8 group were significantly reduced. In addition, the ETN@Fe_7S_8 group exhibited a substantial number of fibroblasts and maintained intact skin tissue, as determined by H&E staining (Fig. 3F). This finding indicates a reduction in inflammation and recovery of the infected wounds. Subsequently, we assessed the expression of cytokeratin ($CK10^+$ and $CK14^+$) and proliferating ($Ki67^+$) cells in skin tissues by immunofluorescence staining (IF). CK10 and CK14 serve as markers for the differentiation of keratinocytes [43], whereas Ki67 is essential for skin repair processes [44]. Our results showed an increased expression of CK10 and CK14 (Fig S7) and a higher number of $Ki67^+$ cells (Fig S8) in the skin tissue on days 3 and 7 following ETN@Fe_7S_8 treatment compared with those in the PBS control, indicating a more rapid cell proliferation and healing response in the wounds following ETN@Fe_7S_8 administration. Furthermore, the scratch assay indicated that ETN@Fe_7S_8 significantly enhanced in vitro HaCaT cell migration by 35% at 24 h, 80% at 48 h, the migration of HaCaT cells on 48 h (Figure S9). Overall, the results indicate that ETN@Fe_7S_8 is a promising candidate for enhanced wound healing by curbing infection and facilitating cytokeratin formation.

Hemostasis is the first step in wound healing. Recently, new hemostatic materials that promote wound healing have been developed [45]. To detect the in vivo hemostatic activity of ETN@Fe_7S_8, we strategically harnessed the rabbit auricular vein hemorrhage model and mouse liver hemorrhage model, serving as quintessential experimental models. Because the concentration of ETN@Fe_7S_8 with the best antibacterial effect was 500 μg/mL, we used this concentration in the hemostasis model. In hemorrhagic auricular vein sites ETN@Fe_7S_8 recovered with a nominal volume of blood being absorbed by the cotton pledger (Figs. 3G). Conversely, rabbits receiving only saline, and lacking ETN@Fe_7S_8, had increased blood loss, accompanied by an continuous hemorrhagic episode lasting 4 min (Figs. 3H-I). In addition, the hemostatic effects of ETN@Fe_7S_8 were confirmed in the mouse liver hemorrhage model corroborated the expeditious hemostatic competence of ETN@Fe_7S_8 (Figs. 3J–L). Furthermore, the bleeding volume and hemostasis time in the ETN group were significantly longer, indicating enhanced hemostatic capability of ETN because of the modification. Collectively, these findings highlight the potential of ETN@Fe_7S_8 as a novel therapeutic tool to address the complex interplay between hemostasis and wound healing.

ETN@Fe_7S_8 suppresses inflammation via ferrous iron and polysulfide

The inflammatory phase is an important component of the wound-healing process, during which immune cells and inflammatory mediators perform essential functions in tissue repair [46, 47]. On day 3, the presence of a large number of macrophages at the wound site indicated an active inflammatory response; however, on day 7, there was a marked reduction in macrophages, indicating a resolution of the acute inflammatory phase (Figs. 4A-B). An increase in $Gr1^+$ cells in the ETN@Fe_7S_8 group by day 3, in contrast with that in the PBS group, indicated a strong neutrophilic reaction, which was associated with improved local antibacterial defense. On day 7, a notable decrease in $Gr1^+$ cells indicated a waning inflammatory phase and a shift toward the proliferative stage of wound repair (Figs. 4C-D). Increased TNF-α and IFN-γ levels in the ETN@Fe_7S_8 group indicated a pronounced reduction in inflammation, which facilitated wound healing (Figs. 4E-F). These M1 polarization-associated cytokines, including IL-6, TNF-α, and IL-12, are typically reduced during the late inflammatory phase of wound healing to accelerate the healing process (Figs. 4G-I). Conversely, there was an increase in the expression of M2 polarization-associated cytokines, such as IL-10, Arg-1, and YM-1, which suppressed the production of pro-inflammatory cytokines and promoted the resolution of inflammation (Figs. 4J-L). This variation in macrophage polarization reflects a balance in the inflammatory response, preventing excessive tissue damage and facilitating the repair and remodeling phases of wound healing.

Ferrous iron potentially aids in eliminating the cells responsible for inflammation, which in turn, decreases the release of inflammatory mediators and cellular damage [41, 48]. Polysulfide relieves inflammation by suppressing the phosphorylation and acetylation of p65 NF-κB and STAT3 [48–50]. The MTT assay indicated that the ideal concentrations for mouse mononuclear macrophage cells (Raw264.7) were 100 μg/mL for ETN@Fe_7S_8, 100 μM for $FeCl_2$, and 20 μM for Na_2S_4 (Fig S10). The NF-κB signaling pathway is an important mechanism for orchestrating inflammatory reactions, and p65, a component of the NF-κB protein complex, is a transcription factor that plays a multifaceted role in regulation [51, 52]. We determined the effect of ETN@Fe_7S_8 on inflammatory response in LPS-induced Raw264.7 cells, which is well-established in vitro model for inflammation. Interestingly, although p65 protein levels remained consistent

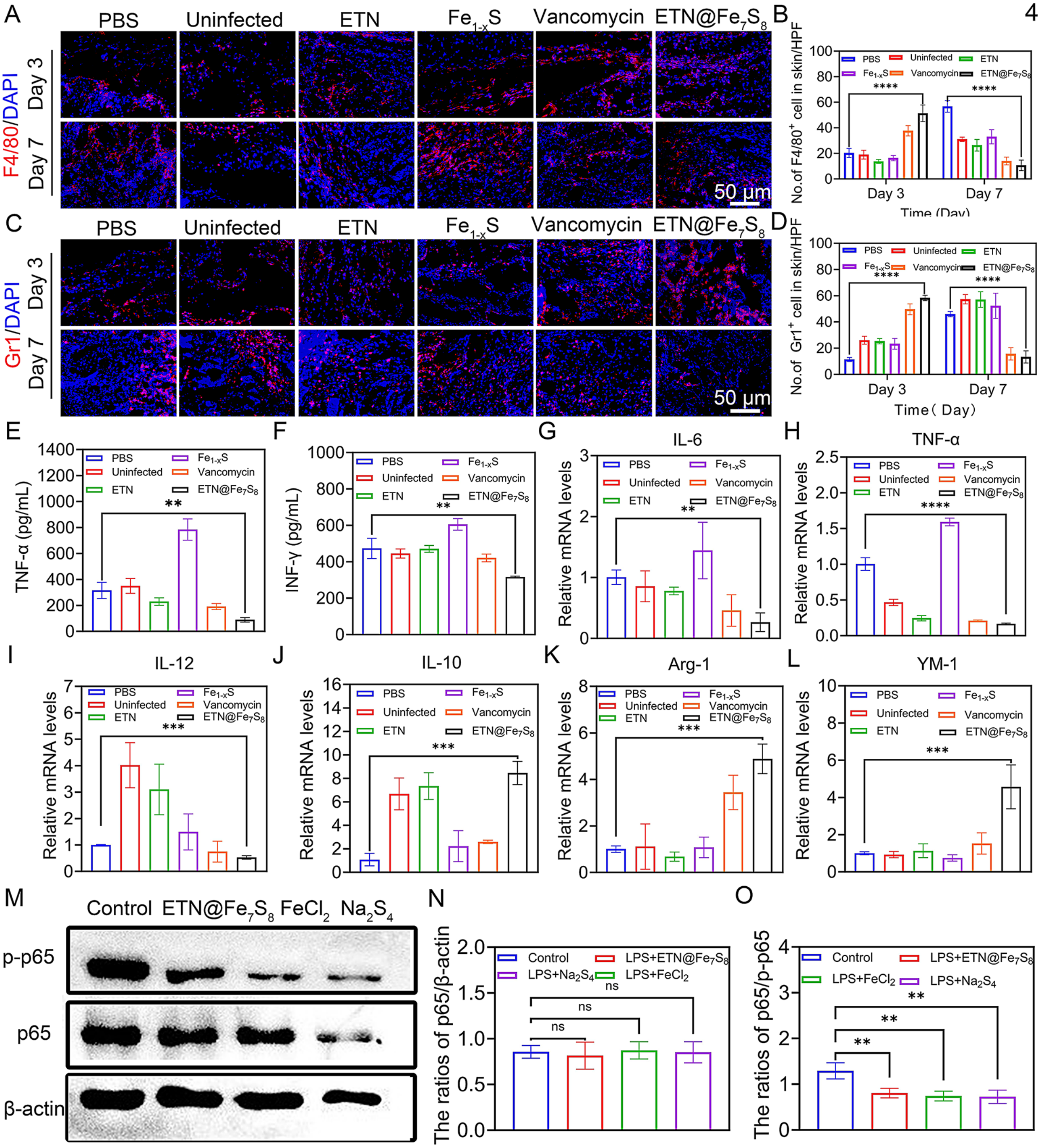

Fig. 4 Anti-inflammatory effect of ETN@Fe_7S_8 in vivo and in vitro. (**A**) IF staining of F4/80 for the wounds on days 3 and 7, and (**B**) the quantitative analysis. (**C**) IF staining of Gr1 for the wounds on days 3 and 7, and (**D**) the quantitative analysis. (**E**) The protein level of TNF-α in wound sites on day 7. (**F**) The protein level of INF-γ in wound sites on day 7. (**G**) The mRNA level of IL-6. (**H**) The mRNA level of TNF-α. (**I**) The mRNA level of IL-12. (**J**) The mRNA level of IL-10. (**K**) The mRNA level of Arg-1. (**L**) The mRNA level of YM-1. (**M**) Western blot analysis of p-p65 and p65 protein levels in LPS-induced Raw264.7 cells. (**N**) The ratios of p65/β-actin. (**O**) The ratios of p65/p-p65. ns: not significant. $^{**}P < 0.01$, $^{***}P < 0.001$, $^{****}P < 0.0001$

across all of the groups, a notable reduction in p-p65 protein levels was observed in the groups treated with LPS in the presence of ETN@Fe_7S_8, $FeCl_2$, or Na_2S_4. This indicates an inhibitory effect on inflammation by both ferrous iron and polysulfide (Figs. 4M-O). Collectively, these findings indicate that ETN@Fe_7S_8, through the modulation of the NF-κB signaling pathway, exerts anti-inflammatory effects, which is a promising approach for therapeutic intervention under inflammatory conditions.

Release of polysulfide from ETN@Fe_7S_8 promotes angiogenesis

Angiogenesis accelerates the rapid healing of infected wounds [53]. To determine the potential role of ETN@Fe_7S_8 in stimulating angiogenesis in MRSA-infected wound models, IF staining was performed. The results indicated a marked increase in CD31 expression, a marker of angiogenesis, in the skin tissues on days 3 and 7 following ETN@Fe_7S_8 treatment. This finding indicates that ETN@Fe_7S_8 effectively enhances angiogenesis as part of the wound-healing process (Figs. 5A-B). Furthermore, the proliferative effect of ETN@Fe_7S_8 on HUVECs was examined. A Trans-well migration assay (Figs S11) revealed that ETN@Fe_7S_8 enhances the migration of HUVECs compared with that in the other groups. In addition, as illustrated in Figs. 5C-D, HUVECs treated with ETN@Fe_7S_8 formed a significantly greater number of lumens as evidenced by in vitro endothelial tube formation assays. This indicates that ETN@Fe_7S_8 promotes cell tube formation, which is important for wound healing.

We have demonstrated that ETN@Fe_7S_8 releases ferrous iron and polysulfide (Figs. 1J-K); however, the specific contribution of these components to angiogenesis is unclear. As shown in Fig S12, we identified the optimal concentration of ETN@Fe_7S_8, $FeCl_2$, and Na_2S_4 for treating HUVECs, which was consistent with the findings in Raw264.7 cells. The scratch assay (Figs. 5E-F) indicated that Na_2S_4 significantly enhanced the migration of HUVEC cells, whereas $FeCl_2$ had a minimal impact on their migration behavior. Consistently, the endothelial cell tube formation assay revealed that HUVEC cells treated with Na_2S_4 formed a greater number of lumens than those treated with $FeCl_2$ (Figs. 5G-H). The cell proliferation assay demonstrated that polysulfides significantly stimulated HUVEC cell proliferation, as quantified by MTT (Fig. 5I). The phosphatidylinositol 3-kinase (PI3K)/Akt signaling pathway plays a critical role in the regulation of diverse cellular functions and is also involved in angiogenesis and erythropoiesis [54, 55]. Our results demonstrated that polysulfides upregulated the expression of key pro-angiogenic factors VEGFA (Fig. 5J). Furthermore, western blotting revealed the activation of the PI3K/AKT signaling axis in HUVEC cells treated with polysulfides and ETN@Fe_7S_8 (Fig. 5K). These observations indicate that enhanced cell tube formation by ETN@Fe_7S_8 is primarily mediated by polysulfide. Further studies are needed to determine the effect of polysulfide on angiogenesis in wound healing in vivo following ETN@Fe_7S_8 treatment.

ETN@Fe_7S_8 demonstrates outstanding biocompatibility *in vitro and in vivo*

To evaluate the biocompatibility of ETN@Fe_7S_8, histological analyses, blood biochemical parameter assessments, and in vitro studies of blood compatibility and cytotoxicity were performed. The histological examinations shown in Fig. 6A revealed that at 7 days post-treatment, the vital organs, including the heart, liver, spleen, kidney, and lungs, showed no obvious necrosis, congestion, or hemorrhage, indicating minimal to no adverse effects on these organs. The serum biochemistry evaluations shown in Figs. 6B-D indicated that the serum concentrations of liver function indicators, including alkaline phosphatase (ALP) and aspartate transaminase (AST), as well as the kidney function indicator UREA, in the animals treated with ETN@Fe_7S_8 were similar to those in the PBS group ($P > 0.05$). These results indicate the excellent biocompatibility of ETN@Fe_7S_8 in both the liver and kidney, which are important for systemic health.

The cell counting kit-8 (CCK-8) assay provided insight into the cytotoxicity of ETN@Fe_7S_8. At a concentration of 250 μg/mL, ETN@Fe_7S_8 did not show any significant cytotoxic effects on Raw264.7 cells or HaCaT cells (Figs. 6E-F), thereby demonstrating favorable safety in these cell types. To ensure the hemocompatibility of the nanomaterial, the hemolysis rate was determined, which is an important parameter to ensure the safety of the nanomaterials. As shown in Fig. 6G, a hemolysis rate at 1000 μg/mL of 3.8% was observed, which is below the standard value of 5% [56]. This percentage indicates the outstanding blood compatibility of ETN@Fe_7S_8 and its importance in preventing adverse hemolytic reactions. Collectively, our findings demonstrate the potential of ETN@Fe_7S_8 as a safe and potent antibacterial nanomaterial that is well-suited for antibacterial treatment with minimal adverse effects on systemic health. The multifaceted assessment of biocompatibility, cytotoxicity, and blood compatibility highlights the value of ETN@Fe_7S_8 as a novel therapeutic agent for antimicrobial therapy.

Conclusion

This study presents a comprehensive evaluation of the ETN@Fe_7S_8 nanocomposite, demonstrating its potential for antimicrobial therapy, particularly against multidrug-resistant bacteria, such as MRSA. Through a series of in vitro and in vivo experiments, we demonstrated that ETN@Fe_7S_8 exhibits remarkable antibacterial

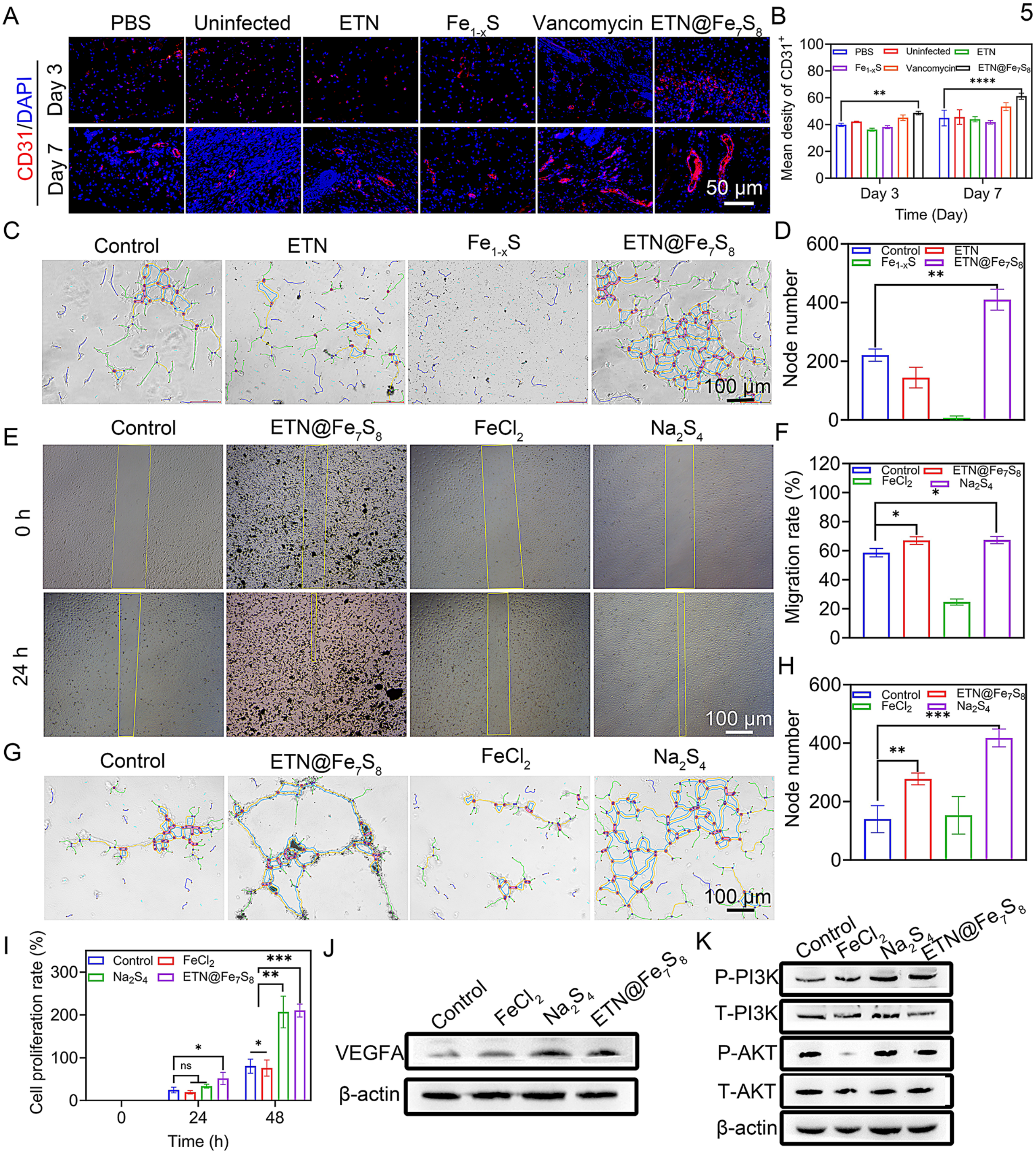

Fig. 5 ETN@Fe$_7$S$_8$ promotes cell migration and tube formation. (**A**) IF staining of CD31 for the wounds on days 3 and 7, and (**B**) the quantitative analysis. (**C**) Images of tube formation with different treatments, and (**D**) quantitative analysis. (**E**) Images of HUVECs migration with different treatments for 0 and 24 h, and (**F**) quantitative analysis. (**G**) Images of tube formation with different treatments, and (**H**) quantitative analysis. (**I**) The cell proliferation rate of HUVEC cells on 0, 24, 48 h. (**J**) Western blot analysis of VEGFA protein levels in HUVEC cells. (**K**) Western blot analysis of AKT, P-AKT, PI3K, and P-PI3K protein levels in HUVEC cells$^*P < 0.05$, $^{**}P < 0.01$, $^{***}P < 0.001$, $^{****}P < 0.0001$

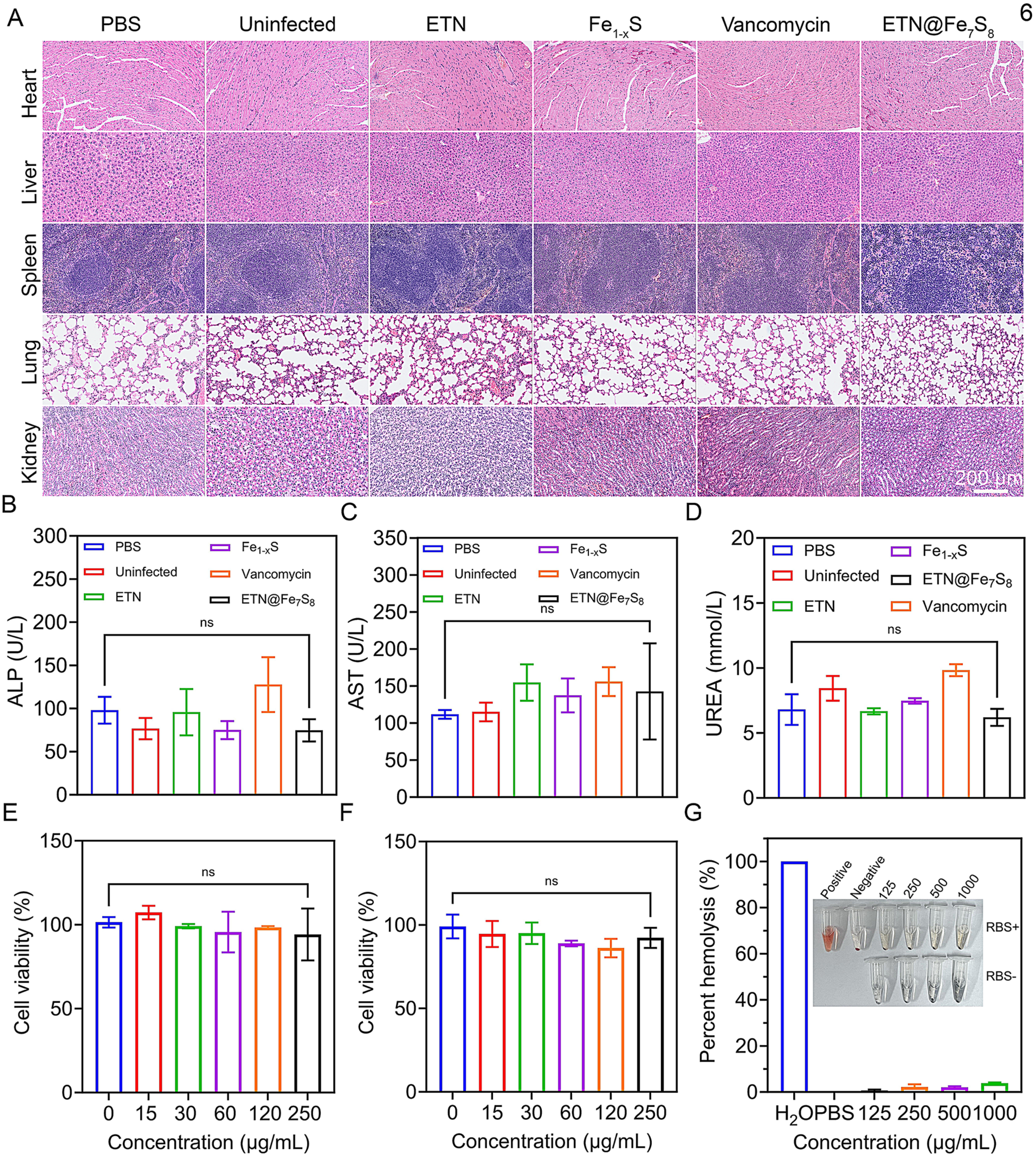

Fig. 6 Biosafety assessment of ETN@Fe_7S_8. (**A**) H&E staining of major organs after different treatments. (**B**) The concentrations of ALP in the serum of the different treatments. (**C**) The concentrations of AST in the serum of the different treatments. (**D**) The concentrations of UREA in the serum of the different treatments. (**E**) Relative viability of Raw264.7 cells with varying concentrations of ETN@Fe_7S_8. (**F**) Relative viability of HaCaT cells with varying concentrations of ETN@Fe_7S_8. (**G**) Hemocompatibility test of ETN@Fe_7S_8. ns: not significant

activity, which was attributed to the release of ferrous iron and polysulfides, two key components of the material. Of these, ferrous iron exerted direct bactericidal effects, whereas polysulfide disrupted bacterial metabolism, enhanced lipid peroxidation, depleted GSH, and ultimately synergized with ferrous iron for bacterial destruction. The hydrothermal synthesis of ETN@Fe_7S_8 presents significant advantages for clinical translation. Unlike other nanozymes relying on complex, energy-intensive processes or toxic solvents, our approach uses biocompatible precursors and mild conditions, reducing environmental risks and facilitating cost-effective scalability. In vivo experiments using a murine model of MRSA infection further substantiated the therapeutic efficacy of ETN@Fe_7S_8. The treatment resulted in accelerated wound healing. And had an excellent coagulation effect on rabbit auricular vein and mouse liver. Both ferrous iron and polysulfide suppressed inflammation, and polysulfide promoted angiogenesis, highlighting the multifaceted role of ETN@Fe_7S_8 in the wound-healing process, which these functional applications are more comprehensive than other nanomaterials (Table S5). Notably, although ETN@Fe_7S_8 shows promise in controlled infection models, its performance in complex chronic wounds remains to be validated. Additionally, long-term biosafety studies are needed to rule out potential iron accumulation or polysulfide-induced cytotoxicity with extended use. Furthermore, the current study primarily focused on MRSA; thus, the nanocomposite's efficacy against other clinically prevalent multidrug-resistant pathogens (e.g., *Pseudomonas aeruginosa* or *Candida* sp.) warrants systematic investigation. Another limitation is the dependency on murine models, which may not fully replicate human wound pathophysiology or immune responses, necessitating validation in higher-order species. Moreover, the material exhibited excellent biocompatibility and minimal systemic toxicity, making it a safe candidate for antibacterial applications. Furthermore, dosage optimization for different wound severities and infection types is required in the future, as excessive iron accumulation could theoretically impair tissue regeneration despite the observed biocompatibility. Future studies will enhance its therapeutic scope by integrating ETN@Fe_7S_8 with drug-loaded carriers (e.g., antibiotics or growth factors) for targeted co-delivery or by optimizing its intrinsic photothermal properties to enable NIR-free activation, thereby broadening applicability across diverse clinical scenarios. Finally, regulatory challenges, including standardized quality control for large-scale synthesis and long-term stability assessments, must be addressed to move toward clinical applicability. In conclusion, the unique properties of ETN@Fe_7S_8, particularly the synergistic action of ferrous iron and polysulfide, indicate its potential value as an advanced antimicrobial treatment.

Abbreviations

ETN@Fe_7S_8	Erythrocyte-templated nanozyme@Fe_7S_8
MRSA	Methicillin-resistant Staphylococcus aureus
GSH	Glutathione
HUVEC	Human umbilical vein endothelial cells
GSSG	Glutathione disulfide
MTT	Methylthiazolyldiphenyl-tetrazolium bromide
LPS	Lipopolysaccharide
SEM	Scanning electron microscope
HAADF	High-Angle Annular Dark Field
EDS	Energy-dispersive X-ray spectroscope
XRD	X-ray diffractometer
TEM	Transmission electron microscope
HaCaT	Human keratinocyte cells
Raw264.7	Mouse mononuclear macrophages cells
DMEM	Dulbecco's Modified Eagle Medium
CFU	Colony-forming units
IF	Immunofluorescence staining

Supplementary Information

The online version contains supplementary material available at https://doi.org/10.1186/s12951-025-03396-w.

Supplementary Material 1

Acknowledgements
We thank the Testing and Analysis Centre at the Institute of Biophysics, Chinese Academy of Sciences (CAS), for characterization of nanomaterials. We thank Xueke Tan for help with TEM samples. We thank Yihui Xu from the Center for Biological Imaging (CBI), Institute of Biophysics, CAS, for help with taking and analyzing CLSM. We thank Prof. Chunli Li (Institute of Microbiology, Chinese Academy of Sciences) for help with SEM characterization.

Author contributions

J.Z. and L.G. designed this study. M.C., T.L., and X.W. conducted experiments and drafted the manuscript. L.G., M.C., T.L., and X.W. analyzed and interpreted the data. J. Z., J.J., and Y. C. revised the manuscript. All authors reviewed the manuscript and declared no competing interests.

Funding
This work was supported by the National Natural Science Foundation of China (U24A20812, 22121003) and the Natural Science Foundation of Beijing (7232102).

Data availability

No datasets were generated or analysed during the current study.

Declarations

Ethics approval and consent to participate

All animal studies were performed following the protocols approved by the Institutional Animal Care and Use Committee of Institutional Animal Care and Use Committee of the Institute of Biophysics, Chinese Academy of Sciences. All animal studies followed ARRIVE guidelines for animal experiments.

Consent for publication

Not applicable.

Competing interests

The authors declare no competing interests.

Received: 10 January 2025 / Accepted: 15 April 2025

References

1. Saeed U, Insaf RA, Piracha ZZ, Tariq MN, Sohail A, Abbasi UA, Fida Rana MS, Gilani SS, Noor S, Noor E, et al. Crisis averted: a world united against the menace of multiple drug-resistant superbugs -pioneering anti-AMR vaccines, RNA interference, nanomedicine, CRISPR-based antimicrobials, bacteriophage therapies, and clinical artificial intelligence strategies to safeguard global antimicrobial arsenal. Front Microbiol. 2023;14:1270018.
2. Walther B, Schaufler K, Wieler LH, Lübke-Becker A. Zoonotic and Multidrug-Resistant Bacteria in Companion Animals Challenge Infection Medicine and Biosecurity. In *Zoonoses: Infections Affecting Humans and Animals.* Edited by Sing A. Cham: Springer International Publishing; 2022: 1–21.
3. Bloom DE, Cadarette D. Infectious disease threats in the Twenty-First century: strengthening the global response. Front Immunol. 2019;10:549.

4. León-Buitimea A, Garza-Cárdenas CR, Garza-Cervantes JA, Lerma-Escalera JA, Morones-Ramírez JR. The demand for new antibiotics: antimicrobial peptides, nanoparticles, and combinatorial therapies as future strategies in antibacterial agent design. Front Microbiol. 2020;11:1669.
5. Salam MA, Al-Amin MY, Salam MT, Pawar JS, Akhter N, Rabaan AA, Alqumber MAA. Antimicrobial resistance: A growing serious threat for global public health. Healthc (Basel Switzerland). 2023;11:1946.
6. Huemer M, Mairpady Shambat S, Brugger SD, Zinkernagel AS. Antibiotic resistance and persistence-Implications for human health and treatment perspectives. EMBO Rep. 2020;21:e51034.
7. Naghavi M, Vollset SE, Ikuta KS, Swetschinski LR, Gray AP. Global burden of bacterial antimicrobial resistance 1990–2021: a systematic analysis with forecasts to 2050. Lancet. 2024;404:1199–226.
8. Lade H, Kim JS. Molecular determinants of β-Lactam resistance in Methicillin-Resistant Staphylococcus aureus (MRSA): an updated review. Antibiot (Basel) 2023, 12.
9. Ambade SS, Gupta VK, Bhole RP, Khedekar PB, Chikhale RV. A review on five and Six-Membered heterocyclic compounds targeting the Penicillin-Binding protein 2 (PBP2A) of Methicillin-Resistant Staphylococcus aureus (MRSA). Molecules 2023, 28.
10. Shalaby MW, Dokla EME, Serya RAT, Abouzid KAM. Penicillin binding protein 2a: an overview and a medicinal chemistry perspective. Eur J Med Chem. 2020;199:112312.
11. Justiz-Vaillant A, Soodeen S, Gopaul D, Arozarena-Fundora R, Thompson R, Unakal C, Akpaka PE. Tackling Infectious Diseases in the Caribbean and South America: Epidemiological Insights, Antibiotic Resistance, Associated Infectious Diseases in Immunological Disorders, Global Infection Response, and Experimental Anti-Idiotypic Vaccine Candidates Against Microorganisms of Public Health Importance. *Microorganisms* 2025, 13.
12. Rasquel-Oliveira FS, Ribeiro JM, Martelossi-Cebinelli G, Costa FB, Nakazato G, Casagrande R, Verri WA. Staphylococcus aureus in inflammation and pain: update on pathologic mechanisms. Pathogens 2025, 14.
13. Bowers S, Franco E. Chronic wounds: evaluation and management. Am Family Phys. 2020;101:159–66.
14. Las Heras K, Igartua M, Santos-Vizcaino E, Hernandez RM. Chronic wounds: current status, available strategies and emerging therapeutic solutions. J Controlled Release: Official J Controlled Release Soc. 2020;328:532–50.
15. Singh S. Nanomaterials exhibiting Enzyme-Like properties (Nanozymes): current advances and future perspectives. Front Chem. 2019;7:46.
16. Bilal M, Khaliq N, Ashraf M, Hussain N, Baqar Z, Zdarta J, Jesionowski T, Iqbal HMN. Enzyme mimic nanomaterials as nanozymes with catalytic attributes. Colloids Surf B Biointerfaces. 2023;221:112950.
17. Nayantara, Kaur P. Biosynthesis of nanoparticles using eco-friendly factories and their role in plant pathogenicity: a review. Biotechnol Res Innov. 2018;2:63–73.
18. Modi SK, Gaur S, Sengupta M, Singh MS. Mechanistic insights into nanoparticle surface-bacterial membrane interactions in overcoming antibiotic resistance. Front Microbiol. 2023;14:1135579.
19. Aflakian F, Mirzavi F, Aiyelabegan HT, Soleimani A, Gholizadeh Navashenaq J, Karimi-Sani I, Rafati Zomorodi A, Vakili-Ghartavol R. Nanoparticles-based therapeutics for the management of bacterial infections: A special emphasis on FDA approved products and clinical trials. Eur J Pharm Sci. 2023;188:106515.
20. Paesa M, Remirez de Ganuza C, Alejo T, Yus C, Irusta S, Arruebo M, Sebastian V, Mendoza G. Elucidating the mechanisms of action of antibiotic-like ionic gold and biogenic gold nanoparticles against bacteria. J Colloid Interface Sci. 2023;633:786–99.
21. Siddiqi KS, Husen A, Rao RAK. A review on biosynthesis of silver nanoparticles and their biocidal properties. J Nanobiotechnol. 2018;16:14.
22. Xu P, Huang W, Yang J, Fu X, Jing W, Zhou Y, Cai Y, Yang Z. Copper-rich multifunctional Prussian blue nanozymes for infected wound healing. Int J Biol Macromol. 2023;227:1258–70.
23. He W, Zhou Y-T, Wamer WG, Boudreau MD, Yin J-J. Mechanisms of the pH dependent generation of hydroxyl radicals and oxygen induced by ag nanoparticles. Biomaterials. 2012;33:7547–55.
24. Din MI, Arshad F, Hussain Z, Mukhtar M. Green adeptness in the synthesis and stabilization of copper nanoparticles: catalytic, antibacterial, cytotoxicity, and antioxidant activities. Nanoscale Res Lett. 2017;12:638.
25. Wang X, Liu T, Chen M, Liang Q, Jiang J, Chen L, Fan K, Zhang J, Gao L. An Erythrocyte-Templated Iron Single-Atom nanozyme for wound healing. Adv Sci (Weinh). 2024;11:e2307844.
26. Wu Z, Xiong Z, Huang B, Yao G, Zhan S, Lai B. Long-range interactions driving neighboring Fe–N_4 sites in Fenton-like reactions for sustainable water decontamination. Nat Commun. 2024;15:7775.
27. Li J, Zhang H, Samarakoon W, Shan W, Cullen DA, Karakalos S, Chen M, Gu D, More KL, Wang G, et al. Thermally driven structure and performance evolution of atomically dispersed FeN_4 sites for oxygen reduction. Angewandte Chemie (International Ed English). 2019;58:18971–80.
28. Guo R, Fang X, Shang K, Wen J, Ding K. Induction of ferroptosis: A new strategy for the control of bacterial infections. Microbiol Res. 2024;284:127728.
29. Fang L, Ma R, Gao XJ, Chen L, Liu Y, Huo Y, Wei T, Wang X, Wang Q, Wang H, et al. Metastable Iron sulfides Gram-Dependently counteract resistant Gardnerella Vaginalis for bacterial vaginosis treatment. Adv Sci (Weinh). 2022;9:e2104341.
30. Xu Z, Qiu Z, Liu Q, Huang Y, Li D, Shen X, Fan K, Xi J, Gu Y, Tang Y, et al. Converting organosulfur compounds to inorganic polysulfides against resistant bacterial infections. Nat Commun. 2018;9:3713.
31. Karkan SF, Davaran S, Rahbarghazi R, Salehi R, Akbarzadeh A. Electrospun nanofibers for the fabrication of engineered vascular grafts. J Biol Eng. 2019;13:83.
32. Karkan SF, Rahbarghazi R, Davaran S, Kaleybar LS, Khoshfetrat AB, Heidarzadeh M, Zolali E, Akbarzadeh A. Electrospun polyurethane/poly (ε-caprolactone) nanofibers promoted the attachment and growth of human endothelial cells in static and dynamic culture conditions. Microvasc Res. 2021;133:104073.
33. Fathi-karkan S, Javid-Naderi MJ, Rahbarghazi R, Rahdar A, Baino F, Keshavarzi Z. Heparinized polyurethane/polycaprolactone nanofibers via oxygen plasma for enhanced endothelialization and angiogenesis in Small-Diameter grafts. BioNanoScience. 2024;15:47.
34. Kim H-K, Ha H-Y, Bae J-H, Cho MK, Kim J, Han J, Suh J-Y, Kim G-H, Lee T-H, Jang JH, Chun D. Nanoscale light element identification using machine learning aided STEM-EDS. Sci Rep. 2020;10:13699.
35. Zhang C, Wei D, Wang F, Zhang G, Duan J, Han F, Duan H, Liu J. Highly active Fe_7S_8 encapsulated in N-doped Hollow carbon nanofibers for high-rate sodium-ion batteries. J Energy Chem. 2021;53:26–35.
36. Li Y, Liu X, Zheng L, Shang J, Wan X, Hu R, Guo X, Hong S, Shui J. Preparation of Fe–N–C catalysts with FeN_x ($x = 1, 3, 4$) active sites and comparison of their activities for the oxygen reduction reaction and performances in proton exchange membrane fuel cells. J Mater Chem A. 2019;7:26147–53.
37. Sun X, Wei P, Gu S, Zhang J, Jiang Z, Wan J, Chen Z, Huang L, Xu Y, Fang C, et al. Atomic-Level Fe-N-C coupled with Fe_3 C-Fe nanocomposites in carbon matrixes as High-Efficiency bifunctional oxygen catalysts. Small. 2020;16:e1906057.
38. Dai W, Shu R, Yang F, Li B, Johnson HM, Yu S, Yang H, Chan YK, Yang W, Bai D, Deng Y. Engineered Bio-Heterojunction confers Extra- and intracellular bacterial ferroptosis and Hunger-Triggered cell protection for diabetic wound repair. Adv Mater (Deerfield Beach Fla). 2024;36:e2305277.
39. Dop RA, Neill DR, Hasell T. Antibacterial activity of inverse vulcanized polymers. Biomacromolecules. 2021;22:5223–33.
40. Sukhbaatar N, Weichhart T. Iron Regulation: Macrophages in Control. In *Pharmaceuticals*, vol. 11. p. 137; 2018:137.
41. Shen X, Ma R, Huang Y, Chen L, Xu Z, Li D, Meng X, Fan K, Xi J, Yan X, et al. Nano-decocted ferrous polysulfide coordinates ferroptosis-like death in bacteria for anti-infection therapy. Nano Today. 2020;35:100981.
42. Shi R, Zhang S, Lang X, Wang T, Qu T, Lai Q, Li L, Yao C, Cai K. Construction of highly active interfacial structures based on Fe^{3+}/Fe^{2+} dynamically regulated MoS_2 to promote polysulfides catalytic conversion for lithium–sulfur batteries. J Energy Storage. 2024;88:111571.
43. Yang S, Sun Y, Geng Z, Ma K, Sun X, Fu X. Abnormalities in the basement membrane structure promote basal keratinocytes in the epidermis of hypertrophic scars to adopt a proliferative phenotype. Int J Mol Med. 2016;37:1263–73.
44. Wang Y, Ding C, Zhao Y, Zhang J, Ding Q, Zhang S, Wang N, Yang J, Xi S, Zhao T, et al. Sodium alginate/poly(vinyl alcohol)/taxifolin nanofiber mat promoting diabetic wound healing by modulating the inflammatory response, angiogenesis, and skin flora. Int J Biol Macromol. 2023;252:126530.
45. Guo B, Dong R, Liang Y, Li M. Haemostatic materials for wound healing applications. Nat Rev Chem. 2021;5:773–91.
46. Li D, Liu Z, Zhang L, Bian X, Wu J, Li L, Chen Y, Luo L, Pan L, Kong L, et al. The LncRNA SNHG26 drives the inflammatory-to-proliferative state transition of keratinocyte progenitor cells during wound healing. Nat Commun. 2024;15:8637.

47. Raziyeva K, Kim Y, Zharkinbekov Z, Kassymbek K, Jimi S, Saparov A. Immunology of acute and chronic wound healing. Biomolecules. 2021;11:700.
48. Lee K-J, Ulrich N, Kim KP, Choi G-J, Kim JW, Kim J, An E-K. Fe^{2+}: Fe^{3+} molar ratio influences the Immunomodulatory properties of maghemite (γ-Fe_2O_3) nanoparticles in an atopic dermatitis model. ACS Appl Bio Mater. 2021;4:1252–67.
49. Kim WY, Won M, Koo S, Zhang X, Kim JS. Mitochondrial H_2S_n-Mediated Anti-Inflammatory theranostics. Nano-micro Lett. 2021;13:168.
50. Sun H-J, Xiong S-P, Cao X, Cao L, Zhu M-Y, Wu Z-Y, Bian J-S. Polysulfide-mediated sulfhydration of SIRT1 prevents diabetic nephropathy by suppressing phosphorylation and acetylation of p65 NF-κB and STAT3. Redox Biol. 2021;38:101813.
51. Sun X, Cao S, Mao C, Sun F, Zhang X, Song Y. Post-translational modifications of p65: state of the Art. Front Cell Dev Biology. 2024;12:1417502.
52. Guo Q, Jin Y, Chen X, Ye X, Shen X, Lin M, Zeng C, Zhou T, Zhang J. NF-κB in biology and targeted therapy: new insights and translational implications. Signal Transduct Target Therapy. 2024;9:53.
53. Li Y, Xu T, Tu Z, Dai W, Xue Y, Tang C, Gao W, Mao C, Lei B, Lin C. Bioactive antibacterial silica-based nanocomposites hydrogel scaffolds with high angiogenesis for promoting diabetic wound healing and skin repair. Theranostics. 2020;10:4929–43.
54. Zhang Y, Zhang H, Zhang B, Ling Y, Zhang H. Identification of key HIF-1α target genes that regulate adaptation to hypoxic conditions in Tibetan chicken embryos. Gene. 2020;729:144321.
55. Abdurahman A, Li X, Li J, Liu D, Zhai L, Wang X, Zhang Y, Meng Y, Yokota H, Zhang P. Loading-driven PI3K/Akt signaling and erythropoiesis enhanced angiogenesis and osteogenesis in a postmenopausal osteoporosis mouse model. Bone. 2022;157:116346.
56. Zhang K, Xian Y, Li M, Pan Z, Zhu Z, Yang Y, Wang H, Zhang L, Zhang C, Wu D. Gelable and adhesive powder for lethal Non-Compressible hemorrhage control. Adv Funct Mater. 2023;33:2305222.

Publisher's note